Materials Today Bio 28 (2024) 101216

Contents lists available at ScienceDirect

Materials Today Bio

journal homepage: www.journals.elsevier.com/materials-today-bio

A water strider-inspired intestinal stent actuator for controllable adhesion and unidirectional biofluid picking

Lihao Zhang [a,1], Lehao Ren [b,1], Sunlong Li [a,1], Minli Xiong [c], Yue Cao [a], Yufei Chen [a], Weipeng Lu [a], Cihui Liu [a,*], Shengzheng Luo [d,e,**]

[a] Center for Future Optoelectronic Functional Materials, School of Computer and Electronic Information/School of Artificial Intelligence, Nanjing Normal University, Nanjing, 20024, China
[b] Department of Critical Care Medicine, Union Hospital, Tongji Medical College, Huazhong University of Science and Technology, Wuhan, 430022, China
[c] Outpatient Department of Shanghai University of International Business and Economics, Shanghai, 210620, China
[d] Department of Gastroenterology, Ningde Municipal Hospital, Ningde Normal University, Ningde, Fujian, 352100, China
[e] Department of Gastroenterology, Shanghai General Hospital, Shanghai Jiaotong University School of Medicine, 650 Xin SongJiang Road, 201620, Shanghai, China

ARTICLE INFO

Keywords:
Colloidal crystals hydrogel
Intestinal stent
Miniature actuator
Controllable adhesion
Unidirectional biofluid picking

ABSTRACT

Soft-bodied aquatic organisms exhibit extraordinary navigation and mobility in liquid environments which inspiring the development of biomimetic actuators with complex movements. Stimulus-responsive soft materials including hydrogels and shape-memory polymers are replacing traditional rigid parts that leading to dynamic and responsive soft actuators. In this study, we took inspiration from water strider to develop a biomimetic actuator for targeted stimulation and pH sensing in the gastrointestinal tract. We designed a soft and water-based Janus adhesive hydrogel patch that attaches to specific parts of the intestine and responds to pH changes through external stimulation. The hydrogel patch that forms the belly of the water strider driver incorporates an inverse opal microstructure that enables pH responsive behavior. The hydrogel patch on the water strider's leg uses a sandwich structure of Cu particles to convert light into heat and bend under infrared light to mimic the water strider's leg simulating the efficient and steady movement of the water strider's leg which transporting the biological fluid in one direction. This miniature bionic actuator demonstrates controlled adhesion and unidirectional biofluid delivery capabilities, proving its potential for targeted stimulus response and pH sensing in the gastrointestinal tract, thus opening up new possibilities for medical applications in the growing field of soft actuators.

1. Introduction

In nature, soft-bodied aquatic organisms such as squid, fish, and turtles exhibit remarkable navigational and independent mobility in liquid environments [1–4]. Inspired by these creatures, the development of bionic actuators that can mimic their complex movements and behaviors has become a highly anticipated area of research [5–8]. Traditional rigid actuators are now being replaced by soft actuators built from stimulus-responsive soft materials including hydrogels, liquid crystal polymers, and shape-memory polymers [9–14]. Compared with traditional actuators composed of rigid parts, soft actuators developed from stimulus-responsive soft materials such as hydrogels, liquid crystal polymers and shape memory polymers can dynamically and actively respond to various stimuli among which soft actuators driven by a mixture of light, electric field, magnetic field and biology are still at the forefront of research [15,16]. Zhao's team has developed a magnetically responsive microneedle actuator for intestinal delivery of macromolecular drugs [17–21]. Yin demonstrated a bionic, adaptive, soft-bodied photothermal swimmer capable of actively adjusting its body functions and modes of operation in response to environmental changes [22]. Dong et al. reported a lightweight airborne hydrogel actuator with remarkable properties such as ultra-high speed motion, fast response and extremely high jump height [23]. Hu's team has designed a soft magnetic micro-actuator for targeted drug delivery that can be delivered

* Corresponding author.
** Corresponding author.
E-mail addresses: cihui@njnu.edu.cn (C. Liu), luoshengzheng2007@163.com (S. Luo).
[1] These autors contributed equally to this work.

https://doi.org/10.1016/j.mtbio.2024.101216
Received 22 May 2024; Received in revised form 4 August 2024; Accepted 23 August 2024
Available online 28 August 2024

through a catheter and anchored to tissue [24]. Ye's team has designed a micro-actuator that enables targeted drug delivery and treatment deep within the gastrointestinal (GI) tract in a minimally invasive manner [25]. Despite the progress, it remains a challenge whether these modified drug carriers can effectively locate surgical sites through the thick digestive fluid [26–28]. In addition, existing carrier devices generally focus only on the release of drugs and lack the ability to extract biological liquids from biological tissues. Therefore the development of an effective intestinal shuttle actuator is still highly anticipated.

In this study we took inspiration from water striders which is an extraordinary creature known for its ability to move efficiently across water and biofluid. Our goal is to develop a bionic actuator that mimics a water strider's waterproof legs and sticky pads to achieve targeted stimulation and pH sensing in the intestine [29–32]. To achieve this goal, we designed a soft, water-based Janus adhesive hydrogel patch that adheres to specific points in the intestine and responds to pH changes through external stimulation [33–38,39–50]. The hydrogel patch consists of a combination of water-soluble polymers and cross-linkers with the ability to absorb and retain large amounts of water and biofluid [51,52]. This property enables the patch to conform to the contours of the intestine while maintaining strong adhesion even in the presence of digestive fluid.

To mimic the water strider's ability to walk on water, we integrated hydrogels containing inverse opal microstructure into the actuator structure. These microstructures allow the actuator to move efficiently and stably while also facilitating the one-way transport of biological fluids through the body and responding to changes in pH. Infrared is also used to precisely control the legs of the water strider actuator allowing it to attach to the intestinal wall and absorb intestinal fluid (Fig. S1). The specificity of the Janus structure allows the legs of the water strider actuator to bend and deform when subjected to light and heat, thus better adhering to the inner wall of the gully-ridden intestine. And due to changes in the intestinal wall environment such as the occurrence of local lesions, the pH value of its intestinal fluid will also change. By absorbing intestinal fluid and recording pH through the water strider actuator, the condition of the intestinal wall can be captured very carefully and accurately providing reliable support for subsequent treatment (Fig. 1).

Taking inspiration from the water strider's natural adaptability, we developed a micro-bionic actuator with controlled adhesion and one-way liquid delivery capabilities. The flexible Janus adhesive hydrogel patch effectively adheres to specific points within the intestinal tract and responds to pH changes through external stimuli. This innovation has the potential for intestine-targeted stimulus-response adhesives and pH

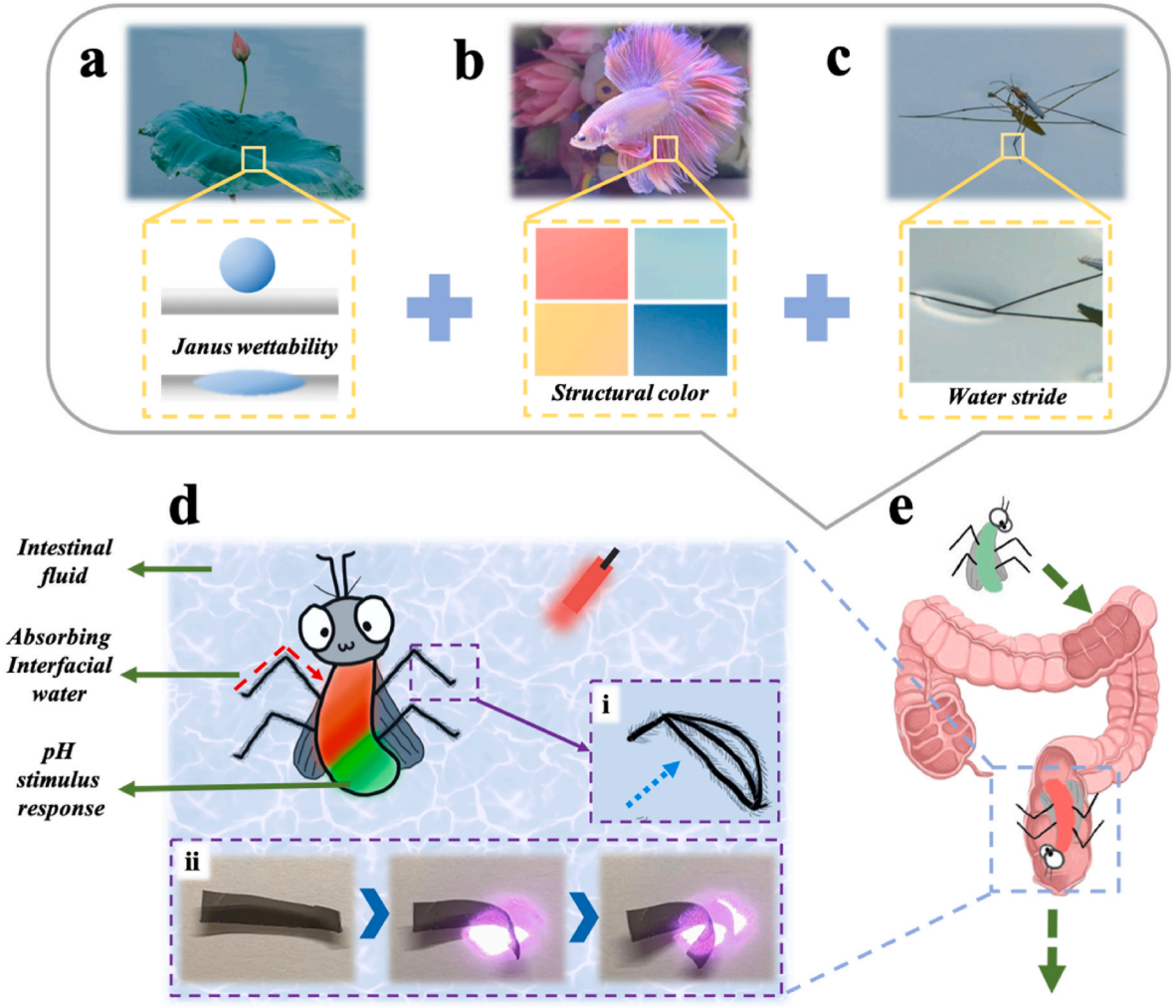

Fig. 1. Program for a polybio-inspired Janus-wetting robotic device combining the advantages of a stimulus-responsive structural color membrane and a candle soot coating. (a) Wettability of Janus from lotus leaves showing superhydrophobic and superhydrophilic capabilities on opposite surfaces. (b) The body structure color of a fighting fish built on a photonic crystal structure. (c) Due to the excellent hydrophobicity of its feet, water striders stand on the surface of the water. (d) A logical diagram of how a hydrogel water strider works inside the intestine: intestinal fluid flows from the water strider's toe to the water strider's abdomen, where a pH detector is loaded to change color according to the pH value of the intestinal fluid and is able to deform under near-infrared light. (e) Schematic diagram of hydrogel water strider discharged after entering the intestinal work.

sensing opening up new possibilities for medical applications. As the field of soft robotics continues to evolve, we believe our research contributes to the development of more versatile and adaptable soft actuators for a variety of applications in the future.

2. Experimental section

2.1. Materials

The monomers of the hydrogels were acrylic acid (≥99 % purity, AA, Sigma Aldrich) and N-isopropylacrylamide (>98 % purity, NiPAAm, Sigma Aldrich). N,N′-methylenebisacrylamide (≥99.5 % purity, BIS, Sigma Aldrich) and ammonium persulfate (≥98 % purity, APS, Sigma Aldrich) were used as cross-linking agent and thermal initiator respectively. 9.72 mmol NiPAAm, 0.48 mmol AA, 0.81 mmol BIS, 0.29 mmol APS and 34.7 mmol deionized water were mixed. Solutions of different pH values were prepared by mixing water with citric acid and trisodium citrate respectively. Polyurethane (average molecular weight of about 16800) was purchased from Mackun. Soot-coated glass slides were placed in a desiccator in which two beakers were filled with about 2 mL of TEOS and HCl, respectively. SiO_2 nanoparticles were self-prepared. Hydrofluoric acid (HF) was obtained from the Aladdin Industrial Corporation. All reagents were of analytical grade and used as received. Simulated Intestinal Fluid (SIF) was purchased from Phygene. Simulated Intestinal Fluid is mainly composed of phosphates, trypsin, etc. and has a pH of 6.8.

2.2. Fabrication of Janus wettability membrane

Hydrogel water strider actuators were multilayered structures of PU/P (NiPAAm-bis-AA), Cu particles, PAM and PDMS/Candle soot.

Stand-alone inverse opal was fabricated using the sacrificial template method. The opal templates were assembled by vertical deposition of a silica latex suspension synthesized by the research group at a concentration of about 0.5 wt% and a latex diameter of 300 nm under constant temperature and humidity conditions. The polymer was infiltrated into the silica opal template by dip-coating. PDMS and curing agent were mixed at 10:1, stirred well and left to stand until the bubbles disappeared completely, and the mixed PDMS solution was poured onto the silica opal template. The PDMS/silica composite film was cured in an oven at 70 °C for 2 h until fully cured. The cured PDMS/silica composite film was immersed in hydrofluoric acid (HF) solution to etch the silica microspheres to form a PDMS film with an inverse opal structure. The dried PDMS antiproteinite film was fixed above the flame at a distance of about 1–2 cm so that the candle smoke was uniformly deposited on the surface of the film.

An appropriate amount of acrylamide (AAm) was dissolved in deionized water to a concentration of 20 % (w/v). An appropriate amount of N,N′-methylenebisacrylamide (MBAA) was added to the acrylamide solution to a concentration of 0.5 % (w/v), and mixed homogeneously, then ammonium persulfate (APS) was dissolved in deionized water to a usual concentration of 0.5 % (w/v). Then the Cu particles were uniformly mixed therein and left at room temperature for 1 h to fully react the mixture to form a hydrogel, and the hydrogel was washed repeatedly with deionized water to remove unreacted monomers and other impurities.

2.3. Characterization

The sensing and moving processes were recorded with a digital camera. Color photos were taken on a digital camera (Canon5D Mark II, Japan). SEM images were obtained from a field emission scanning electron microscope (FE-SEM, HitachiS-3000N, Japan). In situ reflectance spectra were collected by a fiber optic spectrophotometer (Ocean Optics, Inc., HR 2000 UV–vis–NIR).

2.4. Statistical analysis

Statistical analysis was performed using Origin 2018 software and Microsoft Excel 2021. All experiments in this study were repeated at least three times for each group and all quantitative data are expressed as mean ± standard deviation (SD). Differences between groups were determined by a one-way ANOVA test. Significance was set to 0.05 (95 % of confidence interval).

3. Results and discussion

3.1. Preparation of the abdomen of water strider actuators

In a classical experiment, the Janus wettable structured color membrane was fabricated first by copying a silica colloidal crystal template as shown in Fig. S2a. The flexible layer exhibits a periodic porous inverse opal structure (Fig. 2a-b). Candle soot was introduced into the upper layer of the prepared inverse opal scaffolds to impart wettability characteristics to the PU/P(NiPAAm-bis-AA) inverse opal Janus membrane. Inverse opal membranes with Janus wettability were finally obtained where the bottom layer of the inverse opal scaffold was superhydrophilic and the top layer of the flexible polymer coated with candle soot and silica shell was superhydrophobic.

The Janus membrane prepared has distinctive optical features due to the well-ordered inverse opal structure on the bottom surface of the membrane which gives the PU/P (NiPAAm-bis-AA) inverse opal structure a distinctive structural color. This is caused by the photonic band gap (PBG) in which light of a specific frequency is prohibited from being transmitted and optionally reflected. Under normal incidence of the beam, position of the reflection peaks could have been reckoned by Bragg's formula:

$$\xi = 1.633\ a n_{average} \quad (1)$$

In which ξ is the reflection peak wavelength, a is the centroid-to-centroid for the distance among neighboring nanoparticles and $n_{average}$ is the refractive index of the material averaged over time. Compared to the reflected wavelength of the original opal at 650 nm, the respective reflection peak of the inverse opal is blueshifted to around 530 nm (Fig. 2c). The reason for this lies in the fact that the membrane is made of ordered honeycomb pores with a void size of about 240 nm which is a contraction of about 10 % compared to the diameter of the sphere (about 260 nm). In addition, based on Eq. (1), position of the reflection peak λ is related to the $n_{average}$ when the center-to-center distance between neighboring nanoparticles is kept constant. Hence the inverse opal photonic crystals demonstrate diverse reflection peaks and correspondingly vibrant structural colors when the refractive index of the surrounding environment changes (Fig. 2d).

Not only does this macroporous structure contribute to distinctive hydrophilic properties of the membranes besides providing vivid structural colors. The prepared PU/P(NiPAAm-bis-AA) inverse opal exhibits Janus wettability and strong affinity on superhydrophobic surfaces enabling the membrane to drift stably at the water-air interface due to superhydrophobicity (Fig. 2e). This implies that this membrane is able to cling to the water-air interface whilst remaining stably afloat on its own. The top superhydrophobic surface is composed of candle soot and has a black color when viewed from the top while the bottom surface of the Janus membrane is superhydrophilic and has a distinct structural color when viewed from the bottom [53].

3.2. Preparation of the legs for water strider actuators

A photodynamic soft oscillator with an adaptive oscillation mode that responds to light irradiation of various intensities has been developed. It utilizes a layered structure with the main components being a photothermal actuator consisting of a polymer hydrogel and Cu particles

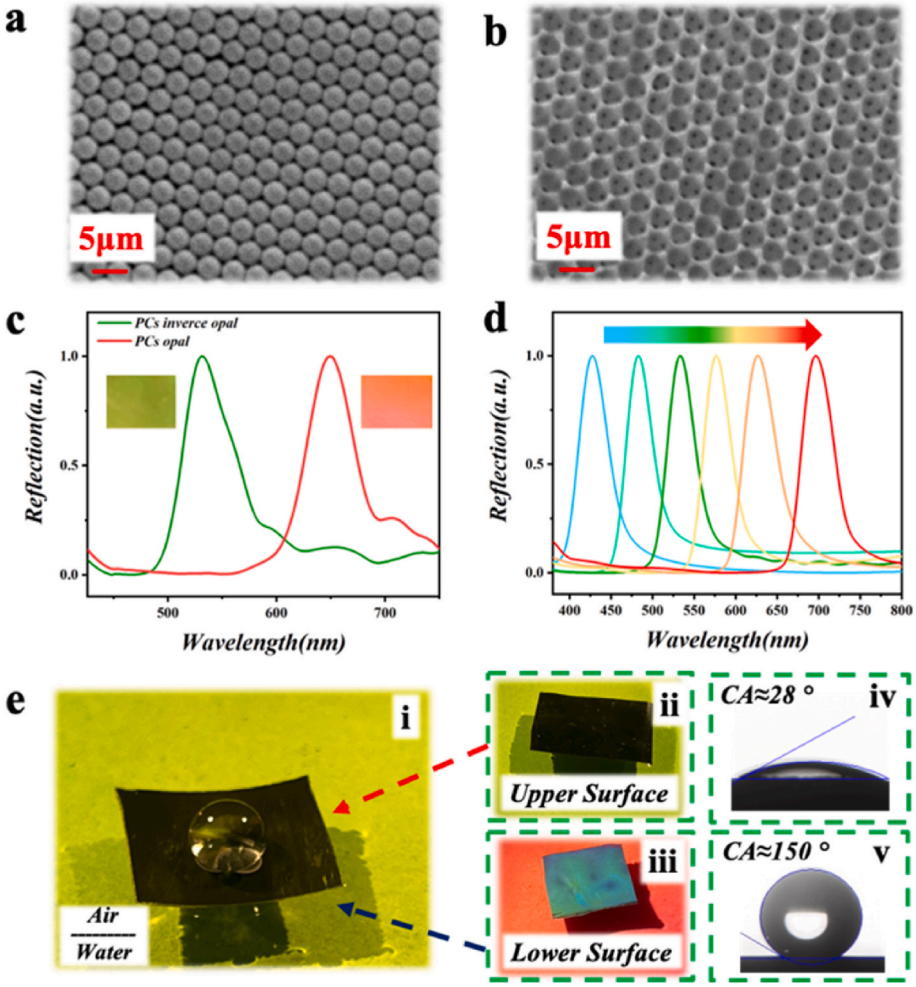

Fig. 2. (a) Scanning electron microscope image of the prepared photonic crystal opal structure. (b) Scanning electron microscope image of the structure of the prepared photonic crystal inverse opal. (c) Optical images of opal and inverse opal and their corresponding reflectance spectra respectively. (d) Reflection spectra of Janus wettable membrane with tunable structural colors. (e) i: Demonstration of the wettability of a prepared Janus membrane floating on water. ii is a photograph of the hydrogel film without the photonic crystal counterstructure and its water contact angle. iii is a photograph of the other side of the hydrogel film, i.e., with the photonic crystal counterstructure and its water contact angle.

(Fig. S2b). Under light irradiation, it heats them up and generates vapor by evaporating the biofluid in the porous hydrogel. The generation of localized vapors results in the formation of bubbles leading to a rhythmic perturbation of the thermodynamic equilibrium of the thin membrane.

The high degree of thermal and mechanical stability enables the three-layer membrane to maintain long-term oscillations in the presence of a continuous water supply. Further demonstration for the potential of this soft evaporator is provided by the design of a water-strider-like swimming actuator that can move continuously and rapidly (at a rate of about 4 body lengths per minute) and achieve highly controllable swimming patterns by adjusting the intensities of the light.

The structure of the three-layer actuator is shown in Fig. 3a. Middle layers consist of Cu particles and PAM hydrogel, which are used to convert light into heat and aerosolize biofluid in the surrounding area. PAM hydrogel is the abbreviation of polyacrylamide hydrogel, which is a kind of hydrogel mainly composed of polyacrylamide. PAM hydrogel is characterised by high water absorption, elasticity, flexibility, biocompatibility and good mechanical strength. The SEM image of the three-layer structure of the hydrogel and the hydrogel layer in the top view are shown in Fig. S3. The PU/P(NiPAAm-bis-AA) layer on the upper part and the polydimethylsiloxane (PDMS) and candle soot layer on the bottom make up the three-layer actuator. Both polymer compounds have different coefficients of thermal expansion, but they are off-the-shelf membrane materials, so the desired structure can be fabricated directly. Since the geometry, shape and size of the actuators can be changed very easily, a systematic study of the designed photothermal oscillator can be carried out. Upon the fact that both PU/P(NiPAAm-bis-AA) and PDMS are hydrophobic as will be discussed later, the fabricated membranes could be floated on the biofluid surface to achieve a function similar to that of an aquatic actuator. Notably the present mechanism holds the potential to broaden to other elastic membranes with different coefficients of thermal expansion thus leaving the door open for a wide variety of adaptive actuators that fulfill application-specific demands. Here we firstly investigate the hydration properties of the hydrogel layer under environmental circumstances. Fig. 3b illustrates the photothermal oscillations caused by vapor generation. In stage i, near-infrared (NIR) irradiation the membrane bend due to the strong coefficient of thermal expansion of PDMS (Movie. S1). As shown in video S1, when the NIR light shines through the intestine to the hydrogel membrane, it is true that it does not make the hydrogel membrane undergo complete movement, but it can make the localized hydrogel membrane undergo regular motion. The reason is that under the irradiation of NIR light, the hydrogel membrane is bent by heat. When the temperature reaches a peak, as the light irradiation continues, the localized temperature increases causing the surrounding biofluid to vaporize, creating bubbles, and when the bubbles expand to the edge of the membrane, the steam is released, allowing the actuator to quickly return to equilibrium. The

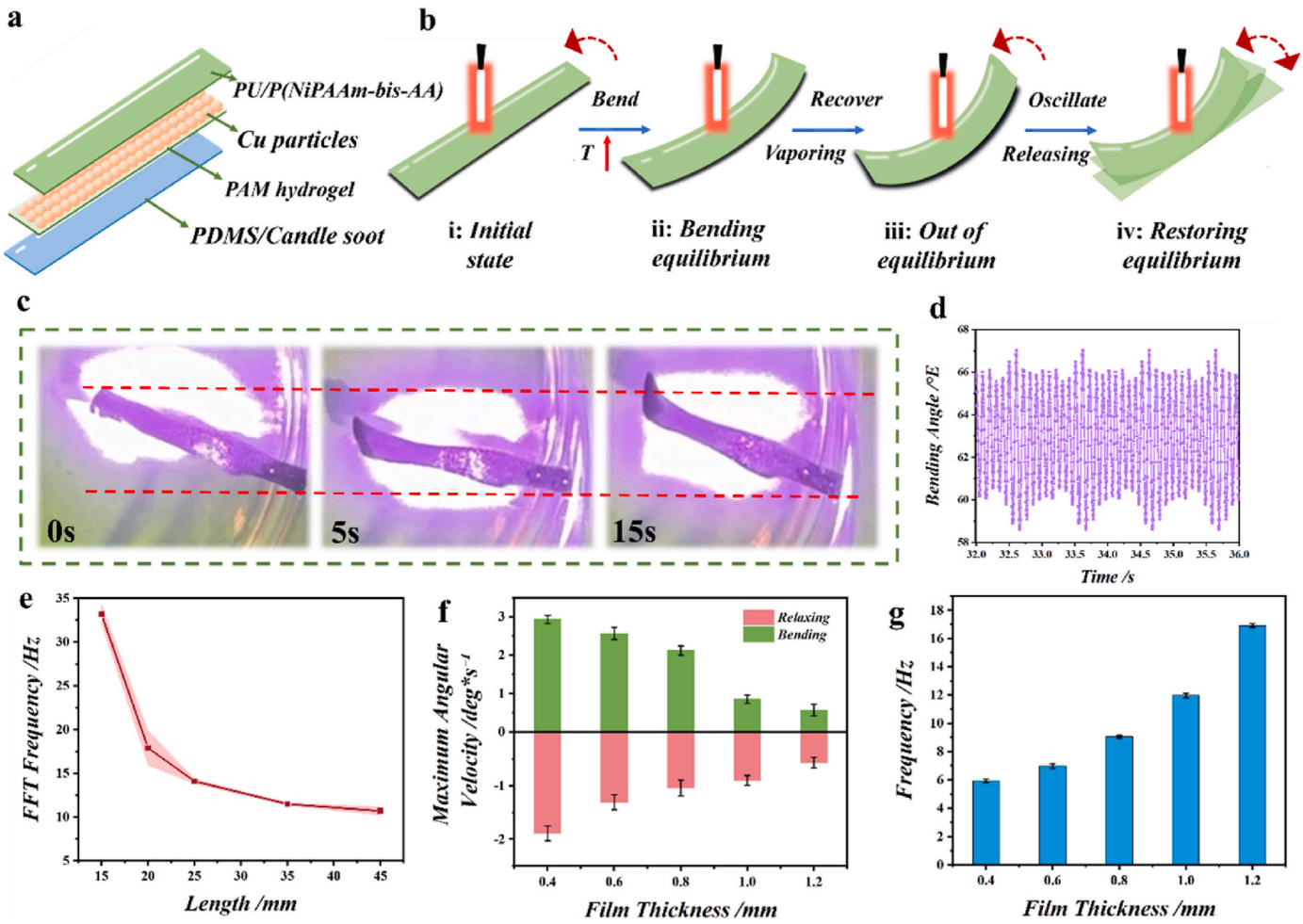

Fig. 3. A photothermal oscillator driven by local steam generation. (a) Schematic diagram of the three-layer structure of the driver. (a) Schematic diagram of the three-layer structure of the driver. (b) Mechanism and operating process of photothermal vapor generation actuating the oscillation of a hydrogel water strider. (c) Diagram of digital photographs displaying the bending of the actuator exposed to near-infrared light. The test was simulated in artificial intestinal fluid. (d) Corresponding FFT of the bending angles. a.u., arbitrary units. (e) Oscillation frequency versus membrane length. (f) Maximum bending and relaxation velocities versus membrane thickness for a three-layer oscillator (a.u., arbitrary units). (g) Function of oscillation frequency as a function of membrane thickness.

continuous generation and release of vapor produces continuous mechanical oscillations within the actuator. So the irradiation of near-infrared light makes the localized regular motion of the hydrogel.

The movement of hydrogel inside the intestine mainly relies on the force generated during the peristaltic movement of the intestine. When the NIR light irradiated the hydrogel membrane, the localised motion of the hydrogel occurred regularly, and its hydrophilic surface was gradually detached from the inner wall of the intestinal tract, and with the peristaltic movement of the intestinal tract, it moved slowly, and after the withdrawal of the NIR light irradiation, the surface temperature of the hydrogel was gradually lowered, and the localised motion was also stopped, and the hydrophilic layer was re-adhered to the inner wall of the intestinal tract. Thus the complete movement of the hydrogel was achieved. The membrane attains an equilibrium state in stage ii with the temperature reaching its peak value. With the continuation of light exposure, the localized elevated temperature aerosolizes biofluid in the surrounding area creating bubbles among the upper PDMS layer and the intermediate hydrogel layer (stage iii). The bubbles function like a gas wedge returning the three-layer actuator marginally to an out-of-equilibrium state. When the bubble expands to the edge of the membrane, the vapor is released causing the actuator to return to equilibrium quickly. The rapid elastic potential energy release initiates the damped resonance cycle of the three-layer actuator. The successive steam production and release produces continuous mechanical oscillations within the actuator. In order to test this hypothesis, an irradiation of the membrane with near-infrared light (2.6W/cm^2) was first performed. During the first 15 s of irradiation, the membrane bends with a monotonically increasing bending angle. The results of this experiment are in accordance with the hypothesis of stage ii. Extending the light irradiation time produces significant oscillations which are associated with rapid and continuous bubble generation inside the membrane [54]. In order to confirm this hypothesis, the film was exposed to near-infrared light (2.6 W/cm^2) to begin with. During the first 15 s of irradiation, as shown in Fig. 3c, the film bends and the bending increases monotonically. The results of this experiment are coherent with the proposed stage ii. Approaching light irradiation generated distinct oscillations which were associated with rapid and continuous bubble generation inside the film. as shown in Fig. 3d, the film was irradiated for the first 15 s with a monotonous increase in bending. The bending angle signal was converted from the time domain to the intensity signal in the frequency domain by using the Fast Fourier Transform (FFT) to calculate the frequency of 10.13 Hz (Fig. 3e). indicating that the film oscillates ~10 times in 1 s.

3.3. Theoretical oscillation models of the photo-thermal oscillators

A model is considered to understand the mechanical oscillations of a three-layer membrane exposed to light irradiation. Hooke's law in

classical mechanics states that the force (F) of a simple harmonic oscillator is proportional to the displacement (x): $F=-kx$, in which k is a positive constant. Among elastic polymers, k has been defined as the stiffness which is expressed as F/x and is used to quantitatively characterize their elastic deformation and to gauge the mechanical properties of the polymer under the action of an external force. The angular frequency (ω_0) of a simple harmonic oscillator can be described as $\omega_0 = (k/m)^{0.5}$ in which m is the quality of the oscillator. Generally a desirable simple harmonic oscillator vibrates with constant amplitude and frequency along the equilibrium position. However mechanical vibrations are usually damped and the amplitude reduces incrementally due to friction, shear strain,and the general conversion of mechanical energy into thermal energy during the actual oscillation process. In order to further characterize the mechanical oscillations of the damped harmonic oscillator, the damping ratio (η) is thus introduced to describe the oscillator frequency with equation 0.5 ζ $(mk)^{-1}$, in which ζ is the damping coefficient.

Thus the frequency of oscillation of a damped resonator (ω_1) is given by $\omega_0\sqrt{1-\eta^2}$. Among the classical mechanical oscillations depending on the value of η, damped harmonic oscillations are of three types, namely overdamped ($\eta > 1$), critically damped ($\eta = 1$) and underdamped ($\eta < 1$) oscillators. Under the two former cases, high damping ratios cause the oscillator to relax to the steady state without oscillating. In the case of insufficient damping, the oscillator relaxes to steady state by continuous mechanical vibration and the amplitude of the oscillation gradually diminishes to zero.

In order to characterize the mechanical oscillations of the three-layer membrane exposed to lighting irradiation, a cantilever beam model was considered, since during the experiment one end of the three-layer membrane was clamped while the other end was relaxed. It is shown in the literature that the angular frequency of the damped harmonic cantilever beam is strongly dependent on the geometry of the beam and can be computed by the following equation:

$$\omega_1 = \frac{\omega_0}{2}\sqrt{4-\frac{\zeta^2 d^4}{\rho SEI}} \tag{2}$$

ω_0 is the angular frequency of the undamped first bending mode, which can be roughly regarded as $3.5(EI/\rho Sd^4)^{0.5}$. Among these expressions, ζ, d, ρ, S, E and I are the damping coefficient per unit cantilever length, cantilever length, cantilever density, cantilever cross-sectional area, Young's modulus and area moment of inertia which translate Eq. (2) into the following formula for the frequency of damped oscillations.

The oscillation frequency (f_1) can be computed from $\omega_1/2\pi$. It can be reasonably assumed that the mechanical oscillations of the three-layer membrane are insufficiently damped because it relaxes to an equilibrium state through successive oscillations of decreasing amplitude. Some of the forces or factors that may dampen the mechanical oscillations include air resistance during the oscillations, inelastic deformation of each polymer layer at high temperatures and possible shear, plastic deformation and displacement at both interfaces of the three-layer membrane. Specifically the three membranes are connected by a PDMS template. The hydrophilic intermediate P(NiPAAm-bis-AA) layer has no adhesion to the hydrophobic apical and underlying layers, resulting in a relaxed interface among these layers. Consequently there may be shear forces and considerable displacement between two adjacent layers which greatly depletes the elastic potential energy and thus dampens the mechanical oscillations. As these facts show, the damping of mechanical oscillations in three-layer membranes is significant and requires the constant generation of vapor to power the sustained mechanical oscillations. Although the membranes are multilayered and the interfaces between each layer are complex, the relationship between the mechanics of the oscillations and the geometry of the membrane can still be explained qualitatively based on the classical theory of harmonic oscillations.

An effect of membrane length on the oscillation frequency was also analyzed. Earlier research forecasts that the oscillation frequency of a simple harmonic oscillator is inversely proportional to the square of the length of the oscillator. In Fig. 3f as we observed, on increasing the membrane length from 15 mm to 45 mm, nevertheless the oscillation frequency decays more slowly than predicted by the harmonic oscillation model. The oscillation frequency (ω_1) of the damped resonance is computed by scaling the frequency of the corresponding resonance with the damping term according to Eqation. S2, $(1-b^2c^4/4degh)^{0.5}$ with positive values ranging between 0 and 1, hence the predicted frequencies are lower than those of harmonic oscillations. The heated area of the illuminant, meanwhile increases with length resulting in the rapid generation of vapor bubbles which in turn increases the magnitude of the driving force. This series of events adds to the frequency of the mechanical oscillations. Thus increasing the length of the membrane produces two opposite effects resulting in an overall slower decay of the oscillation frequency with cantilever length than the predicted frequency of the damped harmonic oscillator.

Membranes undergo the strongest driving force at the onset of bending and the greatest recovering force once the light is turned off resulting in the maximum angular velocity. Rather, as bending and relaxation take place, the membrane builds up bending-induced reaction forces during photothermal actuation and experiences decreasing restoring forces during free relaxation which is the primary reason for the angular velocity decay. By plotting the maximum angular velocity versus the thickness of the membrane, it is found that these two continuous and highly correlated processes are linearly related (Fig. 3g). Afterwards, the mechanical oscillations of these oscillators during photothermal bending are analyzed. The three-layer oscillator was regarded as a cantilever of rectangular cross-section. The oscillatory frequency of the damped resonator decreases with increasing cantilever length (L) with a damping rate greater than $1/L^2$ according to Eq. S2. Further, with increasing film length, more of the film surface was exposed to light increasing the formation of bubbles which could lead to rapid oscillations. These two interacting effects result in higher than expected oscillation frequencies for the three-layer long film. In order to optimally analyze the effect of layer thickness, a rectangular cantilever beam of cross-section b and thickness h is considered. The thickness of the beam is determined by a number of factors. The cross-section (A) and the moment of inertia (I) are calculated as follows: $b \times h$ and $b \times h^3/1^2$, from which it can be predicted that the oscillation frequency increases monotonically with increasing cantilever thickness. This theoretical basis is confirmed by the increasing trend of the measured frequencies for films of different thicknesses (Fig. 3h).

3.4. Biofluid absorption performance of the legs of the water strider actuator

Based on previous experimental work, in order to obtain a better intestinal fluid absorption capacity of hydrogel actuators based on P (NiPAAm-bis-AA) hydrogel and PDMS (Fig. 4a). Detail of the leg of the water strider actuator(Fig. 4b), the size of water strider actuator is about 1 cm * 2 cm. The angle between the feet and the body of the Janus Membrane Robot we have designed is maintained at 90° (shown in Fig. S4). And, the absorption of intestinal fluid by the legs of the water strider actuator is shown in Fig. 4c, evidently the absorption of intestinal fluid is completed within 20 s after the actuator was placed in the biofluid. Hydrogel membranes were also investigated for comparative uptake of PCB opal and PCB inverse opal based biofluid (Fig. 4d). SiO_2 particles were prepared on a slide by horizontal deposition, uniformly coated with P(NiPAAm-bis-AA) hydrogel left to solidify and then peeled off, the membrane with PCs opal was successfully prepared. In contrast, soaking a membrane with PCs opal in 4 % hydrofluoric acid to erode away the SiO_2 particles results in a membrane with PCs inverse opal. It was obvious that the rate of uptake of the hydrogel membrane with PCs inverse opal was much higher than that of the hydrogel membrane with

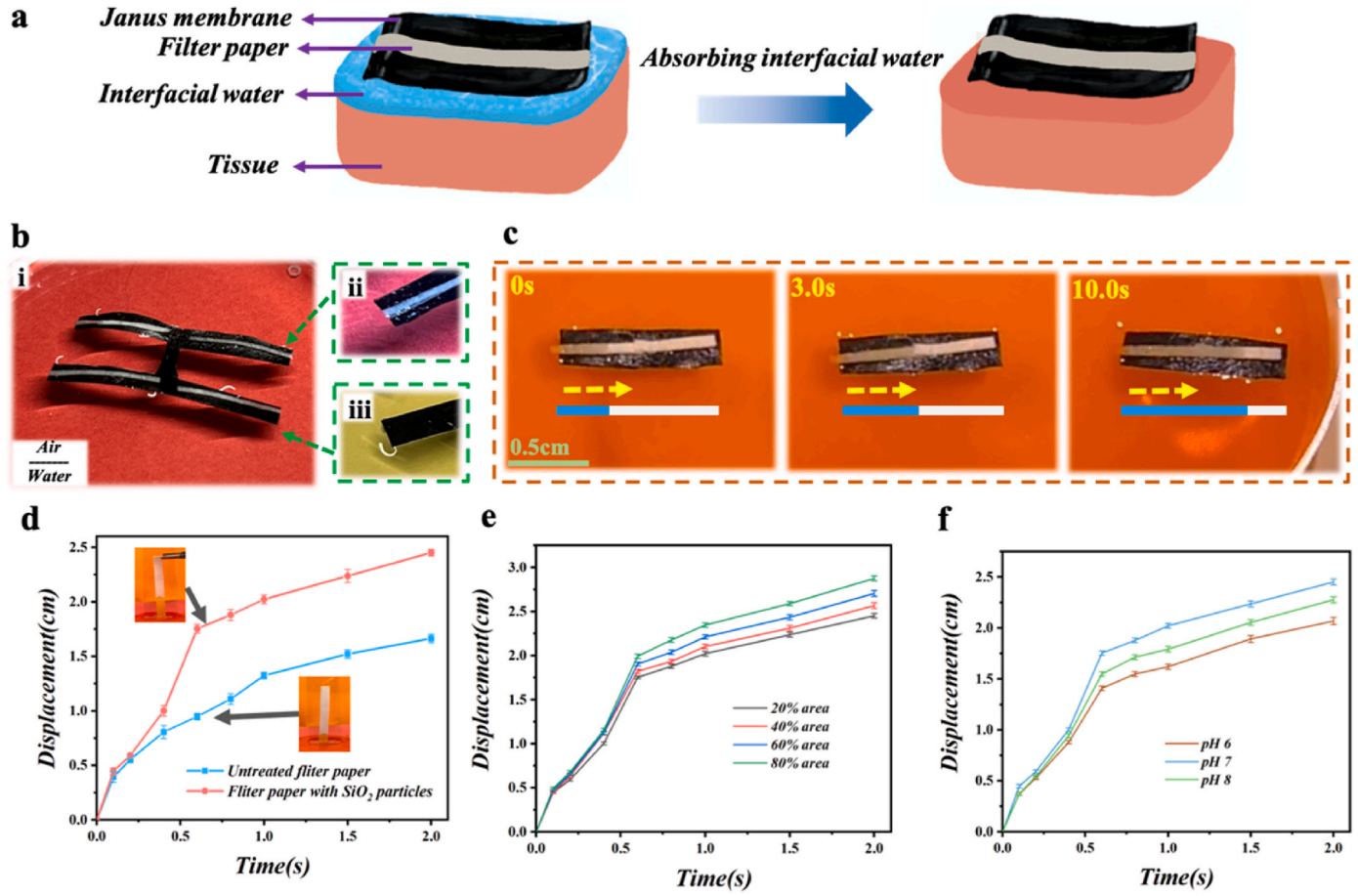

Fig. 4. Absorbent properties of water strider legs. (a) Diagram of the process of absorption of intestinal fluid by hydrogel water striders. (b) Water strider actuator whole figure photograph and leg details. (c) Biofuild absorption experiments on the legs of hydrogel water striders. The test was simulated in artificial intestinal fluid. (d) Comparison of biofliud absorption rate by PCs opal and PCs inverse opal. (e) Comparison of biofluid absorption rates of hydrogel water strider legs with different percentages of PCs inverse opal. (f) Absorption rate of hydrogel water strider in different pH environments.

PCs opal. Comparison of the bioconcentration uptake rates of hydrogel membranes with the PCs inverse opal structure with varying area shares in the legs of the water strider actuator was also investigated by a large number of replicated experiments (Fig. 4e). The data showed that the larger the area ratio, the higher the biofluid absorption rate of the hydrogel membrane with PCs inverse opal. The rate of absorption of liquid by the membrane in different pH environments was also investigated. An optimal biofluidsorption was observed at pH = 7 for hydrogel membranes with PCs inverse opal. Likely, this is related to the better solubility of the fibers under alkaline conditions, whereas under acidic conditions, their absorption properties are significantly reduced. (Fig. 4f).

To illustrate the wettability behavior of droplets in the heating process from the theoretical dimension, a theoretical model describing the transition of the wettability state of the droplets is proposed based on the study of related literature and several rounds of experimental analysis [48]. First we define a series of structural parameters as illustrated in Fig. S5 where D represents the diameter of the film pores, R represents the radius of curvature of the solid-liquid interface, α denotes the dynamic contact angle and β is the other angle. At the onset, the droplets are in a non-wetting state. However as the temperature increases causing the pore size to decrease and under the influence of gravity, the droplet will begin to penetrate into the pore at which point it becomes wetted. In the final stage of the process, the droplet returns to the non-wetting state as the liquid is expelled. From the diagram we can get the expression for R as:

$$R = D/2\cos\beta \tag{3}$$

During the heating process, the wetting phenomenon of the droplets is mainly affected by the combination of Laplace pressure (P_L) and hydrostatic pressure (P_H). The expression for Laplace pressure can be written:

$$P_H = 2\sigma/R = 4\gamma\cos\beta/D \tag{4}$$

where σ represents the surface tension of water and R is the radius of curvature that provides the capillary force. Hydrostatic pressure is calculated from the equation $P_H = \rho gh$ where ρ represents the density of water, g is the acceleration of gravity and h is the height of the droplet. For a given volume of droplets, P_H is a constant directly related to the droplet height. The difference between Laplace pressure and hydrostatic pressure (ΔP) is calculated as:

$$\Delta P = P_H - P_L = \rho gh - 4\gamma\cos\beta/D \tag{5}$$

Penetration of droplets through the pores is only possible if the value of ΔP is positive. Both the P_L and P_H values will tend to increase as the heating process proceeds and therefore their respective determinants of droplet wetting characteristics will also change.

Water striders have to exert various forces in order to float and move on the water surface. In the static state, the forces acting on the superhydrophobic legs consist mainly of buoyancy and surface tension. In the dynamic state, in addition to buoyancy and surface tension, there are additional factors such as drag, inertia and viscous friction. The forces acting on the legs of a water strider when interacting with water can be

categorized into propulsive and drag forces which can be further decomposed into vertical and lateral components.

We can ignore any other factors in dealing with the vertical force of a water strider's legs and focus our attention on the two main factors of buoyancy and surface tension. Archimedes' principle instructs that the buoyancy force (F_P) caused by water pressure is equal to the weight of the water removed by the object. As a result, objects denser than water sink whereas for small objects such as water striders, a capillary effect occurs where the meniscus is squeezed to form a certain curve that provides enough force to keep it afloat (Fig. S6), i.e., the vertical component of surface tension (F_S). To summarize, the vertical component of the net force (F) between the water strider's legs and the water is $F = F_P + F_S$ where surface tension F_T dominates. According to hydrostatic theory, the vertical component of the surface tension F_S is equal to the volume V_S of the water above the free meniscus that is not in contact with the leg multiplied by the density ρ of the water and the gravitational acceleration g (shown in red in Fig. S6) [55].

$$F_s = \rho g V_s \tag{6}$$

By combining Eq. (6) and Archimedes' principle, we get:

$$F = F_P + F_S = \rho g (V_P + V_S) \tag{7}$$

This suggests that the vertical component of the overall force held between the water strider's legs and the surface of the water is equal to the weight of the discharged water. Although this law was derived in a static situation, it still holds roughly true in dynamic processes.

3.5. Water strider actuators in the intestinal tract

To validate the distinctive properties of Janus membranes, we performed a comprehensive interfacial equilibrium experiment to explore the interactions of three samples with the air-biofluid interface which included all-side superhydrophobic (ASHB), all-side superhydrophilic (ASHL) and superhydrophobic/superhydrophilic (SHB/SHL) cooperation Janus membranes. The sample was cut into 0.5 cm × 0.5 cm sheets and fixed vertically to a plastic tube. As the membrane is pressurized into the biofluid then pulled back out of the air-biofluid interface, successive images are clearly captured demonstrating details of the liquid adhesion and air trapping conditions present in the sample and air-fluid interface. With regard to ASHB membranes as the ASHB membranes are immersed in the interface, the superhydrophobicity of the membrane prevents the biofluid from completely wetting the superior interface resulting in the formation of an air trap that creates a considerable buoyancy phenomenon. No liquid remains on the bottom surface when the membrane is removed from the interface (Fig. 5a i). This is a clear result of the superhydrophobicity. Meanwhile the ASHL membrane performs the opposite in the interfacial equilibrium test. No air is trapped when the ASHL membrane is inserted into the biofluid surface as both surfaces are completely wetted due to its superhydrophilicity. This limits the de-wetting process of the membrane by the superhydrophilicity of the bottom surface during the withdrawal process causing the liquid to adhere. As a result, there are significant drawbacks to both types of wetting with ASHL membranes being easier to escape but more difficult to entrap in liquids. (Fig. 5a ii).

Intriguingly the SHL/SHB surfaces of the Janus membrane were positioned at the upper and bottom positions respectively. Regarding the interaction of the Janus membrane at the air-biofluid interface, the superhydrophilic/superhydrophobic surfaces were positioned at the lower/upper positions respectively which shows the synergistic effect of the interaction forces (Fig. 5a iii). Significant air traps are observed when the Janus wettable membrane is pressurized on the interface as a liquid-facing superhydrophilic surface. However, a liquid bridge is formed when Janus membrane leaves the biofluid surface. This gives the conditions for the water strider actuator to be able to stay in the lining of the intestine and even move around the lining of the intestine (Fig. 5b).

Given the practical application scenario of the water strider actuator, a set of control tests was designed as we needed the hydrophilic side surface of the brake to be well adsorbed to the intestines and in contrast the hydrophobic side surface on the other side to be virtually non-adsorbent. The results showed that the hydrophilic side of the actuator adhered to the lining of the large intestine for about 8 s in a scenario with continuous simulated intestinal peristalsis by the use of hands (Fig. 5c, Fig. S7 and Fig. S8), while in contrast the hydrophobic side of the actuator adhered to the lining of the large intestine for about half an hour over a period of ten days of testing (Fig. 5d-e. Fig. 5c and **d** shows the adhesion tests of the dorsal and abdominal surfaces of the hydrogel water strider to the intestinal surface, respectively, where the dorsal surface of the hydrophobic layer of the hydrogel water strider adheres poorly to the surface of the intestines due to its Janus properties, while the abdominal surface of the hydrophilic layer adheres well to the surface of the intestines. On the one hand, the hydrophobic layer consists of nonpolar molecules which lack polar functional groups and therefore cannot form hydrogen bonds with water molecules or polar molecules, so the hydrophobic layer has poor adhesion. The hydrophobic layer is usually smooth and lacks a porous structure or rough surface, which makes it difficult to form physical embedding and mechanical interlocking with the intestinal mucus layer, which further reduces its adhesion. On the other hand, the hydrophilic groups in the hydrophilic layer can form hydrogen bonds with the water molecules in the intestinal mucus, which are strong and can significantly enhance the adhesion properties of the hydrogels. The volume contraction of the PNiPAAm hydrogels may also result in the hydrogels filling more tightly into the tiny grooves and irregular surfaces of the tissues, and this physical embedding effect may improve their stability and adhesion on the contact surface. In addition to this, the hydrophilic layer of the hydrogel has good wettability and can rapidly absorb the surrounding liquid to form a hydrated layer, and this hydrated layer may further enhance the adhesion. The reason for this gap is that the water-strider hydrogel actuator abdomen has reverse photonic crystals, a structural surface roughness that increases the surface area of the film in contact with biological tissues and the hydrophilicity helps the hydrogel to form hydrogen bonds with water molecules in the tissues which enhances the adhesion. The volume contraction of the PNiPAAm hydrogel may also lead to a tighter filling of the hydrogel into the tiny grooves and irregular surfaces of the tissues and this physical embedding effect may improve its stability and adhesion on the contact surface(Fig. 5d-e. Meanwhile a video was shot to demonstrate this control experiment in full (Movie. S2-3).

3.6. Stress movement of water strider actuators

In order to investigate further the application of Janus wettable membranes, we floated a piece of prepared water strider actuators in an 'l'-shaped waterway and recorded their real-time signals under different stimuli. The experiment was designed to simulate the movement of Janus membranes in the intestine based on their interfacial floating properties and stimulus responsiveness. The citric acid solution was injected into the channel from the 'l'-shaped end using a peristaltic syringe pump where the membrane was initially positioned as shown in Fig. 5f. The whole experimental procedure is shown in Movie.4. It is clear that the water strider hydrogel actuator can move autonomously to the lesion according to the Marangoni force. The result of this experiment matches our conception. With increasing citric acid concentration, the Janus membrane directly shifted from the lower citric acid concentration to the higher side which can be recorded as a clearly visible marker of the change in pH of the intestinal fluid brought about by the intestinal lesion. This directed displacement is attributed to the Marangoni effect that occurs at the biofluid-liquid interface. There is a surface tension gradient that can create an external force at the surface of the fluid. Marangoni flow is caused by the uneven evaporation of a surfactant solution. The presence of a surface tension gradient naturally causes the fluid to flow away from the region of low surface tension since

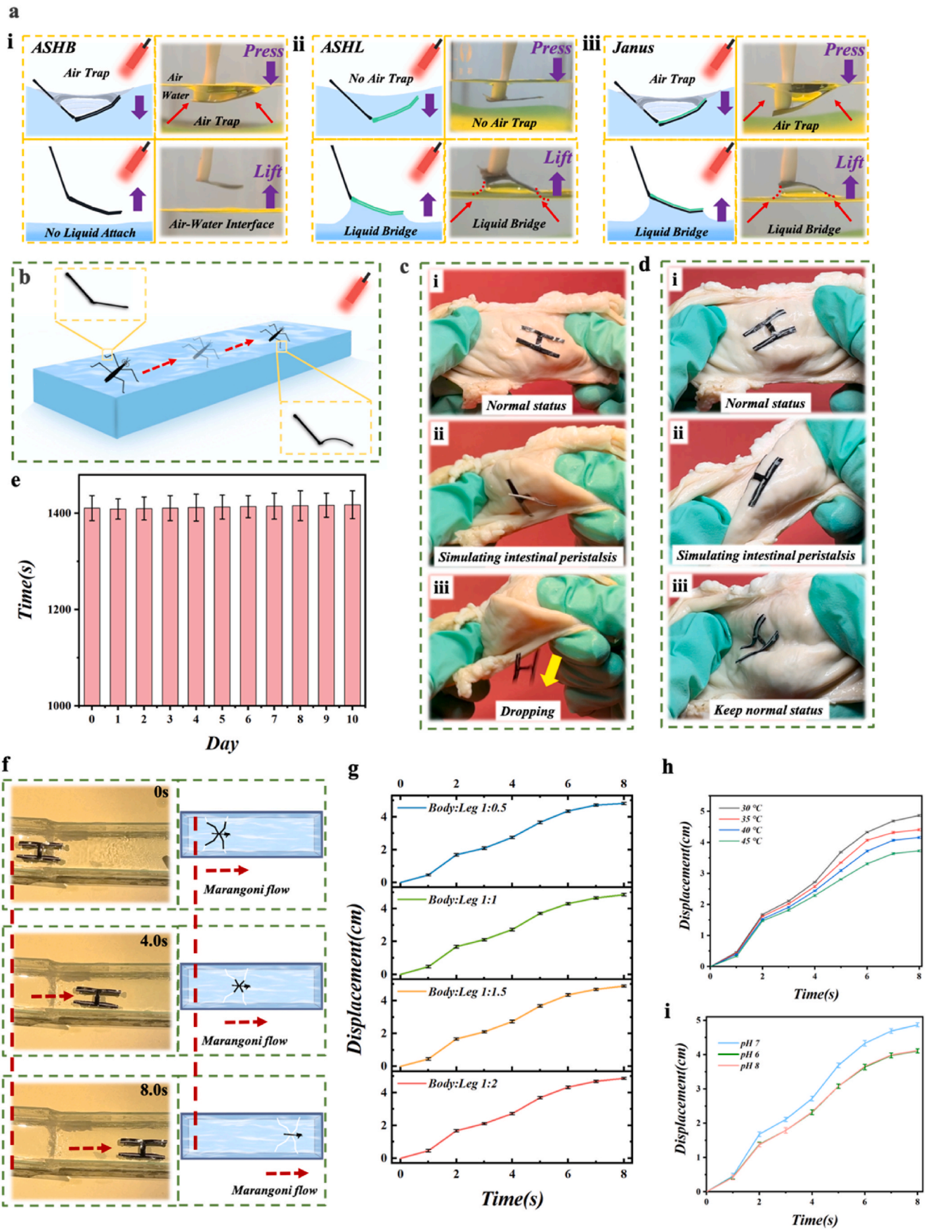

(caption on next page)

Fig. 5. (a) Static schematic and optical image of the interface between the sample membrane and the air/biofuild interface. The test was simulated in artificial intestinal fluid. (i) When the interface is pressed, the ASHB membrane creates an air trap but when the membrane is removed from the biofuild surface, the liquid bridge is not apparent. (ii) Conversely the ASHL membrane does not create air traps but liquid bridges appear. (iii) Air traps and liquid bridges were observed as a result of the Janus membrane. (b) Logical illustration of water strider's movement through the biofuild surface. (c) Intestinal peristalsis was simulated when testing the adhesion of the dorsal surface of the hydrogel water strider and (d) the abdominal surface to the intestinal surface and it is clear that the abdomen has good adhesion compared to the dorsal surface of the hydrogel water strider. (e) Data on the adhesion of the abdominal side of the hydrogel water strider to the intestinal surface when manually simulating intestinal peristalsis for ten consecutive days of testing (using artificial intestinal fluids to simulate an intestinal tract 100 % filled with fluid). (f) Movements of the Janus hydrogel water strider under external stimuli in a 'l'-type water channel. (g) Effect of different waist-to-body ratios on the movement rate of hydrogel water striders at the liquid surface. (h) The displacement distance of the Janus film under various types of liquid with different temperature. (i)The displacement distance of the Janus film under various types of liquid with different pH value.

a fluid with high surface tension exerts a greater pull on the surrounding fluid than a fluid with low surface tension.

To further verify this property of the actuator, we tested the stress movement rate at the biofluid surface for different waist ratios of the actuator (Fig. 5g) and the results showed that the actuator with different waist ratios had almost no effect on its stress movement rate. We also verified the rate of movement and dissolution index of the water strider actuator in different temperature environments to mimic the effect of lesions on the temperature of the intestinal tract. The results showed that the actuator movement rate slowed down with increasing temperature (Fig. 5h and Fig. S9a). The reason for this is that when the temperature is lower than the low critical solubility temperature (LCST), the molecular chains in the system move faster; at temperatures higher than the LCST, the molecular chains move slower due to the enhanced hydrophobic effect and the contraction of the hydrogel structure.

In addition we tested the stress movement rate and dissolution index of the water strider actuator on the surface of different pH solutions as shown in Fig. 5i and Fig. S9b. The results indicated that it shifts the fastest in the liquid of pH at 7.0. This is because the actuator is pH-sensitive and at low pH, hydrogen bonding between the carboxyl group of PAA and the acylamino group of PNiPAAm can lead to shrinkage of the hydrogel. At high pH some of the carboxyl groups) are ionized and this may lead to the destruction of the complex. At pH values greater than 8.0, PNiPAAm is a neutral molecule with some ionized PAA chains around the particle surface. Also, we tested the swelling index of the hydrogel actuator in artificial intestinal fluid over time as shown in Fig. S9c. The data show that the hydrogel rapidly reaches the swelling equilibrium in the first 2 h.

3.7. Unidirectional liquid picking test and pH responsiveness

Considering the sliding mode of the actuator, we persistently simulate the peristalsis of the intestine and continuously injected biofluid to simulate the rehydration of the human body during the expulsion of the actuator (Fig. 6a-b and finally the water strider was expelled from the body. The ability of water strider hydrogel actuators to be excreted from the body is due to the self-peristaltic properties of the intestinal tract. Its complete experiment is shown in Movie.5. A twenty-day cyclic self-discharge test of an artificially simulated water-strider hydrogel actuator after placement in the intestine was also tested and the data showed that the actuator maintained stable discharge performance throughout the twenty-day cyclic test (Fig. S10). In the absence of external stimuli, Janus membranes are able to drain from the body while maintaining their integrity due to their sliding properties. Meanwhile, in order to test its mechanical durabilitymand resistance to biodegradation within the intestinal complex environment, we immersed the water strider actuator in an environment of pH = 6 and artificial intestinal fluid for thirty days and sequentially measured and recorded the daily water strider actuator's surface area change (Fig. S11a), and thirty-day cycles were tested for loss of hydrogel actuator discharge after its placement into an artificially simulated intestinal environment (repeating the experiment of Fig. 6b) (Fig. S11b) and final spectral curves (Fig. S11c). Fig. 6b shows a photograph of the hydrogel water strider discharge process. The three photographs show the process of hydrogel water striders being placed into the intestine, moving inside the intestine, and being expelled from the intestine, respectively. Among them, in Fig. ii, a hand is used instead to simulate the peristalsis of the intestines, and a biofluid is continuously injected to simulate the rehydration process of the human body during the expulsion of the actuator, and finally the water strider is expelled from the body. Since the frequency and state of peristalsis of the intestines can indeed be realized by rubbing and pulling the intestines by the hand, and the continuous injection of biofluids can indeed mimic the more realistic situation of the intestines. The mechanical durability of the water strider actuator was demonstrated in this test due to the acid resistance of the PU/P (NiPAAm-bis-AA) hydrogel itself.

We folded the water strider and automatically unfolded it to its usual condition when it entered the intestine since the water strider actuator was introduced into the body through a medical catheter. A self-propulsion test was conducted in different environments, i.e., pH = 6, 7, 8, and air for 20 days respectively (Fig. 6c). The results showed that the self-propulsion speed was almost stable at 0.03s as shown in (Fig. 6d-e). The full demonstration video is shown in Movie.6. The unfolded water strider leg structure can guide the upward bottom-up transfer of biofluids along the path of the legs due to capillary forces. The combination of the colloidal crystal channel and the inverse opal structure creates a synergistic effect that enables droplets to aggregate within the flow channel. This allows the biofluid to ascend and reach the photonic crystal pH detection module at the top, due to the combined guidance of the capillary force and the wettability of the liquid-solid interface. Notably the structural color of the water strider actuator's belly changed dramatically throughout the stimulation response going from green to blue at pH = 6 and from green to red at pH = 8 (Fig. 6f). We tested the bionic actuator's structural color changes during pH changes by placing the actuator in the intestinal environment at different pH conditions, although the color changes in the in vitro experiments were more pronounced in the different pH environments compared to the in vivo tests (Fig. S12).The darkening of the Janus membrane was caused by the solvent mixture's slow shrinking as the injected solvent eventually entered the Janus membrane. The irritating reaction of PU/P(NiPAAm-bis-AA) caused a structural color change on the hydrophilic surface. The refractive index of the intestinal fluid is altered throughout this process, as does the $n_{average}$ of inverse opal. The Janus membranes underwent a general alteration in landmark and morphological dimensions, as illustrated above.

4. Conclusion

In conclusion, we have successfully developed a miniature bionic actuator inspired by the water strider's natural adaptations. Our soft Janus adhesive hydrogel patch exhibits controllable adhesion and unidirectional liquid transportation capabilities enabling targeted stimulus-responsive adhesive and pH sensing in the gastrointestinal tract. This innovation represents a significant advancement in the field of soft-body robotics and holds great promise for diverse medical applications. Moving forward, our work paves the way for the creation of more versatile and adaptable soft-bodied actuators ushering in a new era of sophisticated bio-inspired technologies.

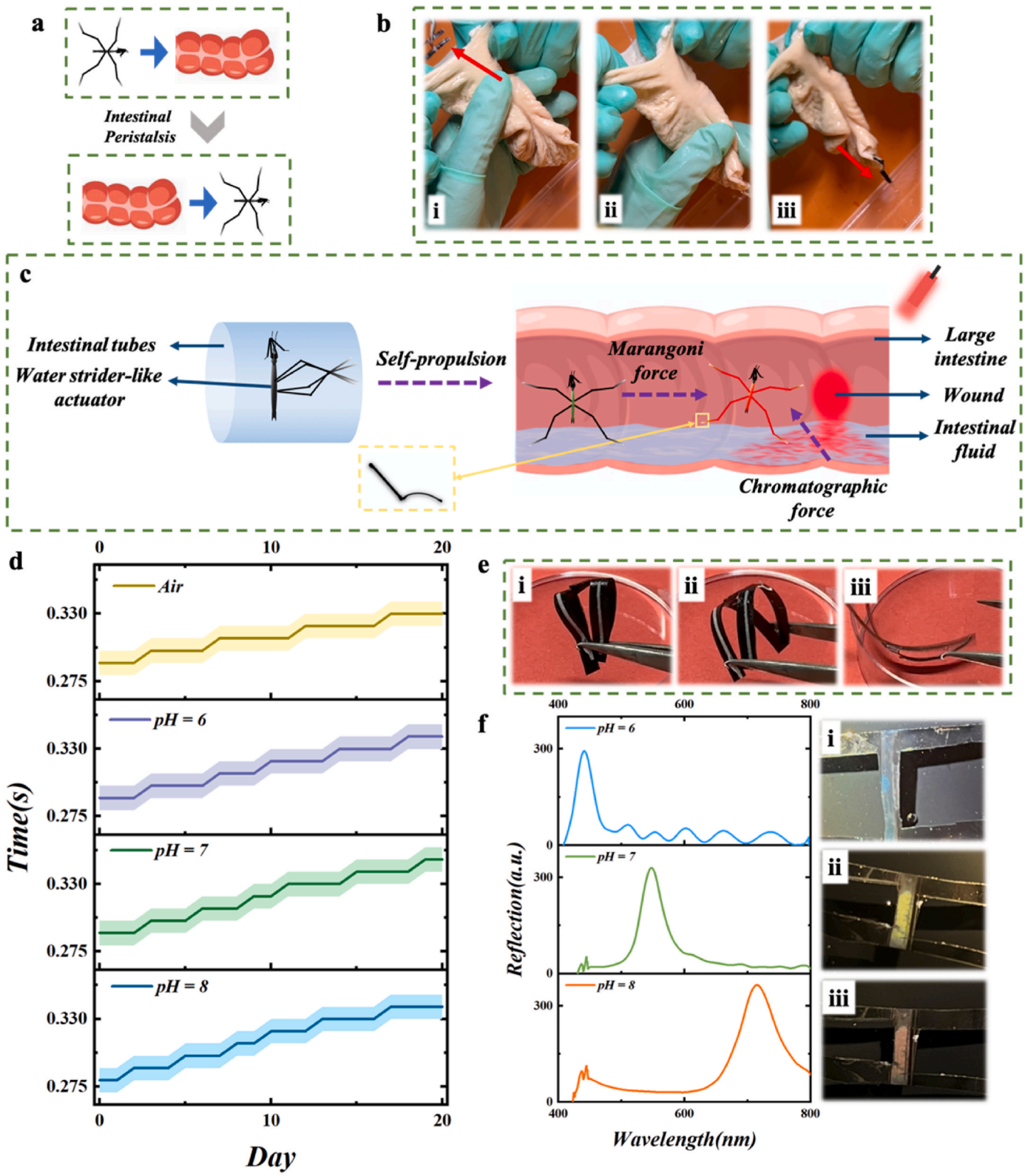

Fig. 6. (a) Logical schematic of the process of expelling a hydrogel water strider after it has been positioned at a fixed point in the intestine. (b) Photographs of the process of expelling a hydrogel water strider. (c) Schematic diagram of water strider actuator feeding into the body and working. (d) The hydrogel water strider was tested in air and pH = 6, 7, 8 respectively, for 20 days of self-propulsion. (e) Photographs of recovery of elastomer after compression. (f) Reflection spectra of the Janus wettability membrane in air and pH = 6, 7, 8 respectively. (i), (ii) and (iii) are the photos of the structural color changes of the water strider actuator under different pH environments, respectively.

Notes

The authors declare no competing financial interest.

CRediT authorship contribution statement

Lihao Zhang: Writing – original draft, Investigation. **Lehao Ren:** Writing – original draft, Investigation. **Sunlong Li:** Investigation. **Minli Xiong:** Software, Resources. **Yue Cao:** Data curation. **Yufei Chen:** Investigation. **Weipeng Lu:** Resources. **Cihui Liu:** Writing – review & editing, Funding acquisition, Conceptualization. **Shengzheng Luo:** Writing – review & editing, Writing – original draft, Funding acquisition, Conceptualization.

Declaration of competing interest

The authors declare no competing financial interests.

Data availability

Data will be made available on request.

Acknowledgements

This work was supported by the National Natural Science Foundation of China (grants 21802074), and the funding from Shanghai Jiao Tong University.

Appendix A. Supplementary data

Supplementary data to this article can be found online at https://doi.org/10.1016/j.mtbio.2024.101216.

References

[1] L. Rosalia, C. Ozturk, J. Coll-Font, Y. Fan, Y. Nagata, M. Singh, D. Goswami, A. Mauskapf, S. Chen, R.A. Eder, E.M. Goffer, J.H. Kim, S. Yurista, B.P. Bonner, A. N. Foster, R.A. Levine, E.R. Edelman, M. Panagia, J.L. Guerrero, E.T. Roche, C. T. Nguyen, A soft robotic sleeve mimicking the haemodynamics and biomechanics of left ventricular pressure overload and aortic stenosis, Nat. Biomed. Eng. 6 (2022) 1134–1147.

[2] J. Li, R. Zhang, L. Mou, M. Jung de Andrade, X. Hu, K. Yu, J. Sun, T. Jia, Y. Dou, H. Chen, S. Fang, D. Qian, Z. Liu, Photothermal bimorph actuators with inbuilt cooler for light mills, frequency switches, and soft robots, Adv. Funct. Mater. 29 (2019) 1808995.

[3] Y. Zhang, D. Yang, P. Yan, P. Zhou, J. Zou, G. Gu, Inchworm inspired multimodal soft robots with crawling, climbing, and transitioning locomotion, IEEE Trans. Rob. (2021) 1–14.

[4] L.X. Lyu, F. Li, K. Wu, P. Deng, S.H. Jeong, Z. Wu, H. Ding, Bio-inspired untethered fully soft robots in liquid actuated by induced energy gradients, Natl. Sci. Rev. 6 (5) (2019) 970–981.

[5] M. Xu, Z. Xu, Z. Jiang, W. Shao, L. Zhang, Y. Chen, Z. Dong, C. Liu, W. Zhang, X. Wan, Biomimicking integrates peristome surface of nepenthes alata onto biliary stents tips, Chem. Eng. J. 454 (2023) 140064.

[6] Q. Lu, Q. Tang, Z. Chen, S. Zhao, G. Qing, T. Sun, Developing an inositol-phosphate-actuated nanochannel system by mimicking biological calcium ion channels, ACS Appl. Mater. 9 (38) (2017) 32554–32564.

[7] H. Yu, H. Qiu, W. Ma, M.F. Maitz, Q. Tu, K. Xiong, J. Chen, N. Huang, Z. Yang, Endothelium-mimicking surface combats thrombosis and biofouling via synergistic long- and short-distance defense strategy, Small 17 (24) (2021) e2100729.

[8] J. Chen, Z. Wang, C. Liu, Z. Chen, X. Tang, Q. Wu, S. Zhang, G. Song, S. Cong, Q. Chen, Z. Zhao, Mimicking nature's butterflies: electrochromic devices with dual-sided differential colorations, Adv. Mater. (2021) e2007314.

[9] Z. Zheng, J. Han, S.O. Demir, H. Wang, W. Jiang, H. Liu, M. Sitti, Electrodeposited superhydrophilic-superhydrophobic composites for untethered multi-stimuli-responsive soft millirobots, Adv. Sci. (2023) 2302409.

[10] W. Shao, L. Zhang, Z. Jiang, M. Xu, Y. Chen, S. Li, C. Liu, Bioinspired conductive structural color hydrogels as A robotic knuckle rehabilitation electrical skin, Nanoscale Horiz 7 (2022) 1411–1417.

[11] Y. Xiang, B. Li, B. Li, L. Bao, W. Sheng, Y. Ma, S. Ma, B. Yu, F. Zhou, Toward a multifunctional light-driven biomimetic mudskipper-like Robot for various application scenarios, ACS Appl. Mater. 14 (17) (2022) 20291–20302.

[12] L. Pancaldi, P. Dirix, A. Fanelli, A.M. Lima, N. Stergiopulos, P.J. Mosimann, D. Ghezzi, M.S. Sakar, Flow driven robotic navigation of microengineered endovascular probes, Nat. Commun. 11 (1) (2020) 6356.

[13] Z. Zheng, H. Wang, L. Dong, Q. Shi, J. Li, T. Sun, Q. Huang, T. Fukuda, Ionic shape-morphing microrobotic end-effectors for environmentally adaptive targeting, releasing, and sampling, Nat. Commun. 12 (1) (2021) 411.

[14] L.Y. Sun, Y.R. Yu, Z.Y. Chen, F.K. Bian, F.F. Ye, L.Y. Sun, Y.J. Zhao, Biohybrid robotics with living cell actuation, Chem. Soc. Rev. 49 (12) (2020) 4043–4069.

[15] G. Pacchioni, A soft Robot that mimics aortic stenosis, Nat. Rev. Mater. 7 (2022) 845.

[16] Y. Si, J. Hu, Z. Dong, Bioinspired magnetically driven liquid manipulation as microrobot, cell rep, Phys. Sci. 2 (6) (2021) 100439.

[17] X. Zhang, L. Sun, Y. Wang, F. Bian, Y. Wang, Y. Zhao, Multibioinspired slippery surfaces with wettable bump arrays for droplets pumping, Proc. Natl. Acad. Sci. 116 (42) (2019) 20863–20868.

[18] Y. Yu, J. Guo, M. Zou, L. Cai, Y. Zhao, Micromotors from microfluidics, Chem. Asian J. 14 (14) (2019) 2417–2430.

[19] X. Zhang, G. Chen, Y. Yu, L. Sun, Y. Zhao, Bioinspired adhesive and antibacterial microneedles for versatile transdermal drug delivery, Research (2020) 3672120.

[20] X. Zhang, G. Chen, F. Bian, L. Cai, Y. Zhao, Encoded microneedle arrays for detection of skin interstitial fluid biomarkers, Adv. Mater. 31 (37) (2019) 1902825.

[21] F.F. Fu, L.R. Shang, Z.Y. Chen, Y.R. Yu, Y.J. Zhao, Bioinspired living structural color hydrogels, Sci. Robot. 3 (16) (2018) 5900–5905.

[22] H. Zhu, B.R. Xu, Y. Wang, X.X. Pan, Z.H. Qu, Y.F. Mei, Self-powered locomotion of a hydrogel water strider, Sci. Robot. 6 (53) (2021) eabe7925.

[23] M. Li, X. Wang, B. Dong, M. Sitti, In-air fast response and high speed jumping and rolling of a light-driven hydrogel actuator, Nat. Commun. 11 (1) (2020) 3988.

[24] X.Y. Hu, Y.T. Zhou, M.Y. Li, J.F. Wu, G.N. He, N.D. Jiao, Catheter-assisted bioinspired adhesive magnetic soft millirobot for drug delivery, Small (2023) 2306510.

[25] Z.C. Ye, L.M. Zheng, J.J. He, J.Z. Lin, Y.R. Chen, H.D. Yu, Y. Wang, W.J. Zhong, S. Handschuh-Wang, S.C. Niu, Z.W. Han, Z.G. Guo, B. Wang, Liquid-metal soft electronics coupled with multi- legged robots for targeted delivery in the gastrointestinal tract, Cell (2024) 100181.

[26] H. Zhu, B. Xu, Y. Wang, X. Pan, Z. Qu, Y. Mei, Self-powered locomotion of a hydrogel water strider, Sci. Robot. 6 (53) (2021) eabe7925.

[27] W. Lin, J. Klein, Recent progress in cartilage lubrication, Adv. Mater. (2021) e2005513.

[28] W. Zhou, P. Xiao, T. Chen, Carbon-based Janus films toward flexible sensors, soft actuators, and beyond, Acc. Mater. Res. 4 (4) (2023) 334–347.

[29] Y. Su, Z. Xiang, X. Song, S. Zheng, X. Xu, Design and optimization of a new anti-reflux biliary stent with retractable bionic valve based on fluid-structure interaction analysis, Front. Bioeng. Biotechnol. 10 (2022) 824207.

[30] Y. Wang, R. Zhao, X. He, Z. Zhang, J. Meng, S. Wang, Water spider-inspired nanofiber coating with sustainable scale repellency via air-replenishing strategy, Adv. Mater. 35 (14) (2023) e2209796.

[31] Z. Jiang, Y. Chen, M. Xu, W. Shao, L. Zhang, C. Liu, Bioinspired superwettable catheters with tunable structural color for efficient drug release monitoring, Adv. Mater. Interfaces 10 (8) (2023) 202202047.

[32] X. Zhang, C. Liu, L. Zhang, L. Jia, M. Shi, L. Chen, Y. Di, Z. Gan, Bioinspired tunable structural color film with Janus wettability and interfacial floatability towards visible water quality monitoring, Adv. Funct. Mater. 31 (2021) 2010406.

[33] Z. Sun, Y. Yamauchi, F. Araoka, Y.S. Kim, J. Bergueiro, Y. Ishida, Y. Ebina, T. Sasaki, T. Hikima, T. Aida, An anisotropic hydrogel actuator enabling earthworm-like directed peristaltic crawling, Angew. Chem. Int. Ed. Engl. 57 (48) (2018) 15772–15776.

[34] H. Jia, J. Flommersfeld, M. Heymann, S.K. Vogel, H.G. Franquelim, D.B. Bruckner, H. Eto, C.P. Broedersz, P. Schwille, 3D printed protein-based robotic structures actuated by molecular motor assemblies, Nat. Mater. 21 (6) (2022) 703–709.

[35] M. Li, L. Yuan, Y. Liu, F. Vogelbacher, X. Hou, Y. Song, Q. Cheng, Bioinspired light-driven photonic crystal actuator with MXene-hydrogel muscle, Cell Rep. Phys. Sci. 3 (6) (2022) 100195.

[36] M. Seale, A. Kiss, S. Bovio, I.M. Viola, E. Mastropaolo, A. Boudaoud, N. Nakayama, Dandelion pappus morphing is actuated by radially patterned material welling, Nat. Commun. 13 (1) (2022) 2498.

[37] J. Zhang, D. Sun, B. Zhang, Q. Sun, Y. Zhang, S. Liu, Y. Wang, C. Liu, J. Chen, J. Chen, Y. Song, X. Liu, Intrinsic carbon nanotube liquid crystalline elastomer photoactuators for high-definition biomechanics, Mater. Horiz. 9 (3) (2022) 1045–1056.

[38] C.-Y. Lo, Y. Zhao, C. Kim, Y. Alsaid, R. Khodambashi, M. Peet, R. Fisher, H. Marvi, S. Berman, D. Aukes, X. He, Highly stretchable self-sensing actuator based on conductive photothermally-responsive hydrogel, Mater. Today 50 (2021) 35–43.

[39] Y.D. Wu, X.G. Dong, J.K. Kim, C.X. Wang, M. Sitti, Wireless soft millirobots for climbing three-dimensional surfaces in confined spaces, Sci. Adv. 8 (21) (2022) e7925.

[40] Yun-Woo Lee, Sungwoo Chun, Donghoon Son, Xinghao Hu, Martina Schneider, Metin Sitti, A tissue adhesion-controllable and biocompatible small-scale hydrogel adhesive Robot, Adv. Mater. (2022) 2109325.

[41] F. Soto, J. Wang, R. Ahmed, U. Demirci, Medical micro/nanorobots in precision medicine, Adv. Mater. (2020) 2002203.

[42] G. Gumuskaya, P. Srivastava, B.Z. Copper, H. Lesser, B. Semegran, S. Garnier, M. Levin, Motile living biobots self-construct from adult human somatic progenitor seed, Adv. Mater. (2023) 2303575.

[43] Y.C. Qu, K.Y. Lu, Y.J. Zheng, C.B. Huang, G.N. Wang, Y.X. Zhang, Q. Yu, Photothermal scaffolds/surfaces for regulation of cell behaviors, Bioact. Mater. 8 (2022) 449–477.

[44] X.D. Zhang, Q. Li, L.F. Li, O.Y. Jiang, T. Wang, J.J. Chen, X.Q. Hu, Y.F. Ao, D. T. Qin, J.J. Zhang, J. Cheng, W. Tao, Bioinspired mild photothermal effect-

reinforced multifunctional fiber scaffolds promote bone regeneration, ACS Nano 17 (7) (2023) 6466–6479.
[45] X.Y. Ge, H. Wen, Y. Fei, R. Xue, Z. Cheng, Y.N. Li, K.Y. Cai, L.Q. Li, M.H. Li, Z. Luo, Structurally dynamic self-healable hydrogel cooperatively inhibits intestinal inflammation and promotes mucosal repair for enhanced ulcerative colitis treatment, Biomaterials 299 (2023) 122184.
[46] X.Y. Liu, Y.Y. Yang, M.E. Inda, S.T.W.J.J. Lin, Y. Kim, X.Y. Chen, D.C. Ma, K. Lu, X. H. Zhao, Magnetic living hydrogels for intestinal localization, retention, and diagnosis, Adv. Funct. Mater. 31 (27) (2021) 2010918.
[47] W.C. Huang, W.J. Wang, W.W. Wang, Y.A. Hao, C.H. Xue, X.Z. Mao, A double-layer polysaccharide hydrogel (DPH) for the enhanced intestine-targeted oral delivery of probiotics, Engineering 34 (3) (2023) 05024.
[48] X.L. Liu, J. Gao, Z.X. Xue, L. Chen, L. Lin, L. Jiang, S.T. Wang, Bioinspired oil strider floating at the oil/water interface supported by huge superoleophobic force, ACS Nano (2012), https://doi.org/10.1021/nn301550v.
[49] J.Z. Ma, H.Y. Lu, X.S. Li, Y. Tian, Interfacial phenomena of water striders on water surfaces: a review from biology to biomechanics, Zool. Res. 41 (3) (2020) 231–246.
[50] B. Xiao, Y. Xu, S. Edwards, L. Balakumar, X. Dong, Sensing mucus physiological property in situ by wireless millimeter-scale soft robots, Adv. Funct. Mater. 34 (8) (2024) 2307751.
[51] Y. Wang, H. Cui, Q. Zhao, X. Du, Chameleon-inspired structural-color actuators, Matter 1 (3) (2019) 626–638.
[52] F.L. Zhang, J.B. Fan, P.C. Zhang, M.J. Liu, J.X. Meng, L. Jiang, S. Wang, A monolithic hydro/organo macro copolymer actuator synthesized via interfacial copolymerization, NPG Asia Mater. 9 (2017) e380.
[53] X.R. Zhang, C.H. Liu, L.L. Zhang, L.N. Jia, M.Q. Shi, L. Chen, Y.S. Di, Z.X. Gan, Bioinspired tunable structural color film with Janus wettability and interfacial floatability towards visible water quality monitoring, Adv. Funct. Mater. (2021) 2010406.
[54] Z.W. Li, N.V. Myung, Y.D. Yin, Light-powered soft steam engines for self-adaptive oscillation and biomimetic swimming, Sci. Robot. 6 (2021) eabi4523.
[55] Y. Xu, B. Xiao, L. Balakumar, K.L. Obstein, X. Dong, Wireless millimeter-size soft climbing robots with omnidirectional steerability on tissue surfaces, IEEE Rob. Autom. Lett. (2023) 5720.